

Article

Experimental Investigation of the Dynamic Response of a Sliding Bearing System under Different Oil Pressure Levels

Zhiguo Feng ¹, Qiang Ding ¹, Yinhui Cai ¹ and Weipeng Sun ^{2,*}¹ CHN Energy Dadu River Repair & Installation Co., Ltd., Leshan 614900, China² State Key Laboratory of Eco-Hydraulics in Northwest Arid Region, Xi'an University of Technology, Xi'an 710048, China* Correspondence: sbxbw2008@xaut.edu.cn

Abstract: A sliding bearing system performs a critical function in a rotating machinery system and provides support for the rotating components. In this paper, a single-rotor experimental rig and a dual-rotor sliding bearing experimental rig were independently established, and the dynamic response of the test systems are investigated. To study the effect of oil pressure levels on the dynamic response of the test systems under the single-rotor system and the dual-rotor system, the vibration response of single-rotor and dual-rotor systems were analyzed by different oil inlet pressures to study the effect of oil pressure levels on the dynamic response of the test systems under the single-rotor system and the dual-rotor system. Among them, the single rotor system under a large oil pressure system is mostly periodic and more stable. While under different inlet oil pressure conditions applied in the experiments, the dynamic motion of the dual-rotor bearing system is relatively stable in both the subcritical and supercritical speed regions. However, the oil whirl and oil whip of the dual-rotor system were observed at the critical speed, which causes the system into unstable multiperiodic motions. In general, this paper can give some insight into the dynamic response of the sliding bearing system influenced by different oil pressure levels.

Keywords: sliding bearing; experimental test; oil pressure level; oil whirl; oil whip; whirl orbit



Citation: Feng, Z.; Ding, Q.; Cai, Y.; Sun, W. Experimental Investigation of the Dynamic Response of a Sliding Bearing System under Different Oil Pressure Levels. *Appl. Sci.* **2022**, *12*, 9759. <https://doi.org/10.3390/app12199759>

Academic Editor: José António Correia

Received: 30 August 2022

Accepted: 25 September 2022

Published: 28 September 2022

Publisher's Note: MDPI stays neutral with regard to jurisdictional claims in published maps and institutional affiliations.



Copyright: © 2022 by the authors. Licensee MDPI, Basel, Switzerland. This article is an open access article distributed under the terms and conditions of the Creative Commons Attribution (CC BY) license (<https://creativecommons.org/licenses/by/4.0/>).

1. Introduction

Support provided by bearings for rotating parts has always been a major problem in the rotating machinery system, such as pumps, hydraulic turbines and compressors. According to the support mode, the bearing can be classified into two types, the rolling bearing, and the sliding bearing. Compared with the rolling bearing, sliding bearings are more widely used in the industrial field due to its significant advantages of low vibration noise, low energy loss, high bearing capacity with low accident rate. The supporting force of the sliding bearing is mainly provided by the lubricating oil in the clearance between the bearing and the shaft. In fact, the lubricating oil continuously features squeezing movement in the sliding bearing. It forms a thin oil film to bear the movement of the rotating shaft, which is responsible for the narrow clearance between the bearing and the shaft journal, as well as the rotation effect of the shaft. The pressure generated by the oil film between the bearing bush and shaft journal can be decomposed into radial force and circumferential force, and the shaft journal is supported by the radial force. For the circumferential force, it is susceptible to cause can the rotor to produce violent lateral vibration and puts at risk the stability of the rotating machinery system because of its consistent direction with the rotating direction. Therefore, the influence of pressure produced by the oil film on the stability of the rotating system has gained more interest among researchers and designers.

The dynamic response of the sliding bearing system is generally solved by the methodology named nonlinear kinetics due to its features of being strongly nonlinear and influenced by some factors such as time and rotating speed. In addition, the dynamic parameters

are bound to affect the vibration response of the sliding bearing system and degrade the performance of the whole system. The boundary conditions perform a critical function in analyzing the pressure field distribution of the oil film towards the sliding bearing system, which can be classified into four types: the semi-Sommerfeld boundary condition, the Sommerfeld boundary condition, the Reynolds boundary condition, and the mass conservation boundary condition. The oil pressure distribution, the size of the cavity region, and its location are directly affected by the above boundary conditions [1–4]. The establishment of a nonlinear oil film force database provides a new solution for efficiently and accurately calculating oil film force and analyzing the dynamic characteristics of the rotor system. The accuracy of the numerical calculation method can be guaranteed by the database retrieval interpolation, as well as improved calculation efficiency [5–8]. Hei [9] obtained the analytical expression of oil film pressure by using the vibrational principle and variable separation method and compared the calculation results with finite element simulation to study the influence of oil inlet pressure and position on oil film pressure distribution and its filled area including the initial edge and rupture edge. Kang [10] calculated the oil film force sliding bearings limited in a finite length by solving the N-S equations and obtained the influence regulation of the degree of eccentricity, journal speed, bearing width-diameter ratio, and action-angle on the rotation subsystem. A database calculation method analyzing the nonlinear oil film force with inlet oil pressure taken into account was proposed by Qin [11] to finitely process the axis velocity and boundary condition of inlet oil pressure. The results show that the method is convenient for solving the rotor's transient operation with more calculation efficiency. Oil pressure distribution for the sliding bearing system with double-oil groove circular bush was calculated by Yu [12], and the influence of oil inlet pressure and journal disturbance speed on the internal flow field of sliding bearing and the bearing capacity were elaborated, which provides a theoretical basis for nonlinear characteristics analysis of rotor system and bearing design. The numerical investigation given by Gao [13] indicated that the maximum pressure in the bearing would be increased by slotting the lower tile. In contrast, the influence of slotting from the upper tile on the oil film pressure is insignificant, but the amount of oil intake will increase. Yang [14] derived an approximate analytical expression of nonlinear oil film force and defined the correlation coefficient in the expression by analyzing and studying the structural parameters of bearings, journal, and lubricating oil. Shi [15] solved the Reynolds equation based on the finite difference method and obtained the distribution of oil film pressure and stress at the bearing bush. In addition, the relationship between the oil film pressure, the stress of bearing bush alloy layer, eccentricity, and the damping parameters are built. Li [16] established calculation models of sliding bearings with three different oil inlet holes, and the oil film bearing capacity, pressure distribution, and oil temperature distribution are analyzed and studied under different oil inlet holes. Wang [17] studied the influence of oil inlet pressure and its position on the dynamic characteristics of axial inlet groove sliding bearings by solving the motion differential equation of the journal center track and determining the critical speed of instability by using the trial-and-error method. The influence of Reynolds numbers at the inlet on the flow structure, internal pressure, and shear force in the oil chamber was investigated by Liu [18] with the PIV velocimetry system and numerical simulation. The numerical results were validated against experimental data. Goryunov [19] provided experimental data of sliding bearings under different inlet pipe arrangements, relative values of inlet pipe pressure, and rotating shaft speed, and analyzed the influence of the inclination of the throttle element shaft on fuel consumption.

The published research on the influence of oil pressure on system stability is mainly based on finite element analysis and theoretical analysis by means of solving the differential equation. However, experimental investigation of the issue is considerably infrequent. In addition, there is limited research available on the dynamic response of rotating systems to the critical conditions of the oil pressure.

The vibration characteristics of the rotor-sliding bearing system are closely related to the inlet oil pressure of the sliding bearing. The innovative points and main research of

this paper are: (1) experimental rigs of a single-rotor system and a dual-rotor system are established innovatively; (2) Through the application of an oil supply system. The vibration characteristics of the single-rotor system and dual-rotor system under different bearing inlet oil pressure were investigated. (3) The dynamic characteristics of the dual-rotor system near the critical speed were analyzed. Its nonlinear characteristics under different inlet oil pressure conditions and the steady operating state were also investigated.

2. Experimental Apparatus and Parameters

In order to carry out the vibration and diagnosis analysis of the rotor system, a dual-rotor test rig with sliding bearings is built (as shown in Figure 1) to investigate the dynamic response. The rotor test bench was built by us after several strength check experiments and critical speed calculations, using materials that are more widely used in industry. The basic parameters of the test bench and the stability of the operation in the experiment have been gradually improved through adjustments. The test rig includes a pedestal, two bearing seats, a motor connected with a shaft, two disks, and an inflow and outflow pipe filled with oil. The length and diameter of the shaft in the rotor system are 0.7 m and 0.02 m. The diameters of the disks are both 0.14 m with a thickness of 0.025 m, and a single disk weighs 3 kg.

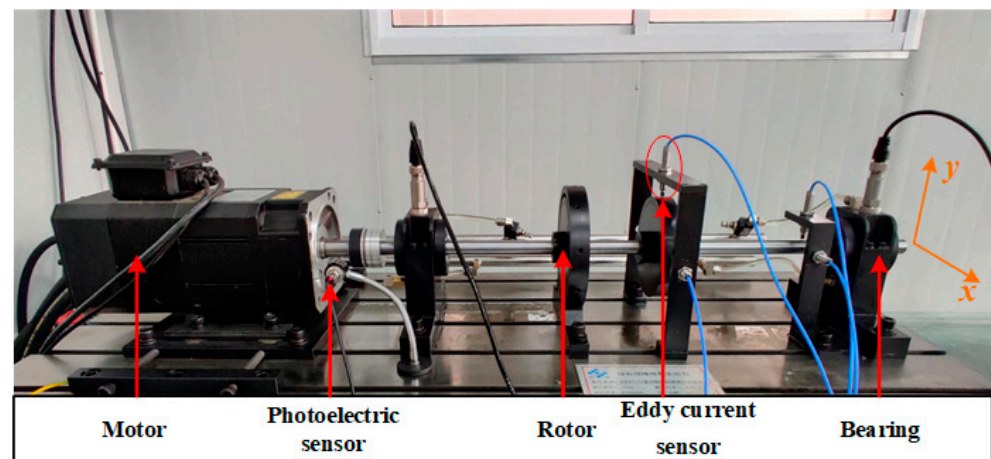


Figure 1. The dual-rotor sliding bearing system test rig.

The rotating speed of the rotor is adjusted through a control cabinet shown in Figure 2, and the connection between the output shaft of the motor and the rotating shaft is implemented by a diaphragm coupler that also provides power to the experimental rotor system. A set of four WT0150 series eddy current sensors is used to capture and feedback the vibration signal from the disk and the shaft in the vicinity of the fault bearing. The sensors spaced by 90° are placed along the X and Y directions, respectively, for the disk and shaft, see Figure 1. In addition, an acceleration sensor installed at the sliding bearing is used to record the rotating speeds of the experimental system, and a photoelectric sensor with a horizontal arrangement is used to record the signals of rotating speed and its phase at the coupler. During the experimental campaign, the variation ranges of the motor rotating speed are from 300 rpm to 6500 rpm, taking into account the experimental design and system stability. The displacement signal caused by system vibration is logged by the HD2000 data acquisition system, sampled at 1024 Hz. At each rotational speed, the sampling duration of the experimental data under investigation is 30 s. The data acquisition system and the sampling interface are shown in Figure 3.

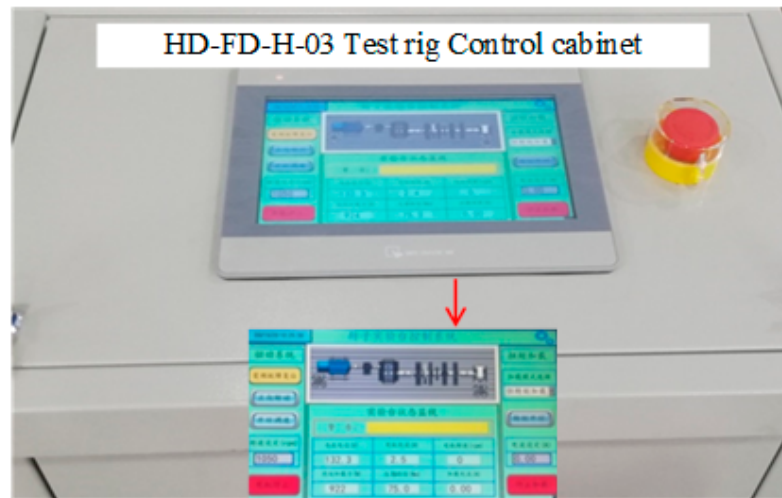


Figure 2. Control cabinet.

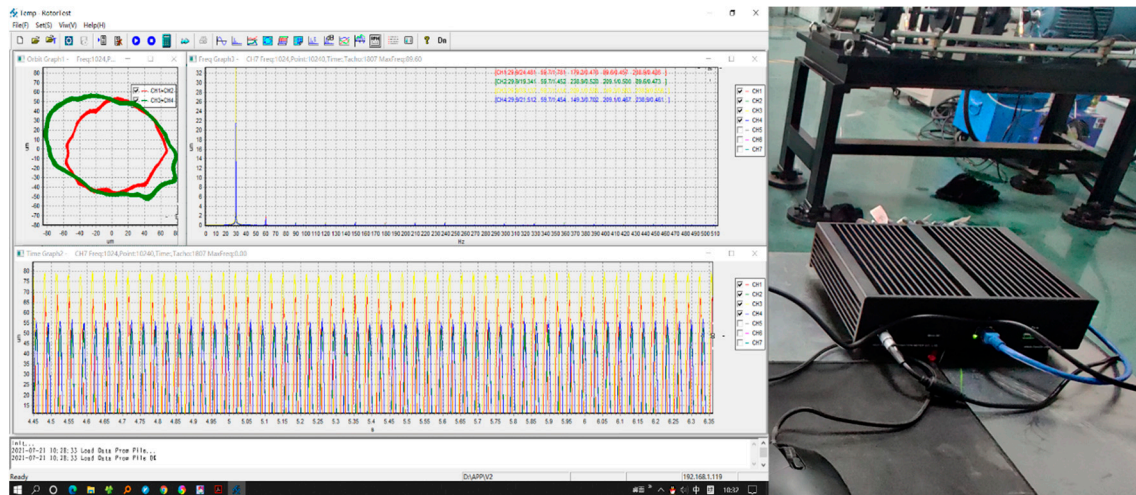


Figure 3. Data acquisition system.

The oil supply system is shown in Figures 4 and 5 shows the physical diagram of the oil tank and oil pressure gauge. (1) 0.18~0.55 K Ω , rated speed 157 rad/s; (2) oil pressure max. 60 bar (6 MPa); (3) oil pipe size inner diameter 6 mm, material stainless steel; (4) oil tank volume is 20 L (with air outlet).

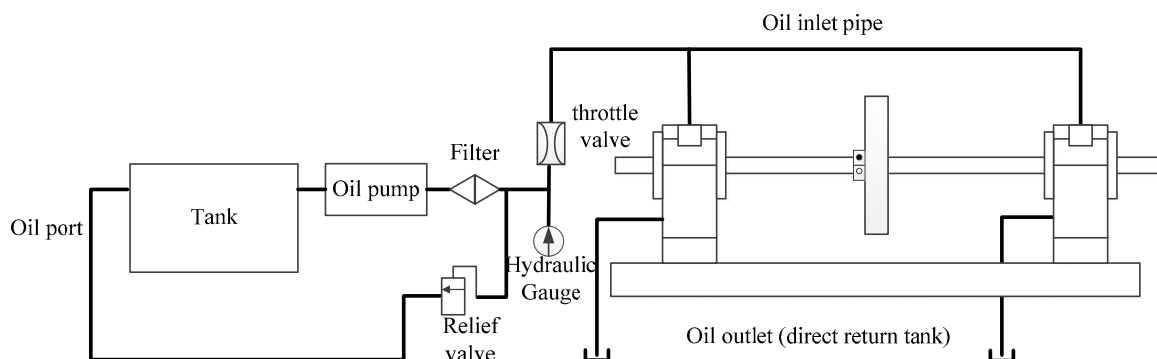


Figure 4. Oil supply device.

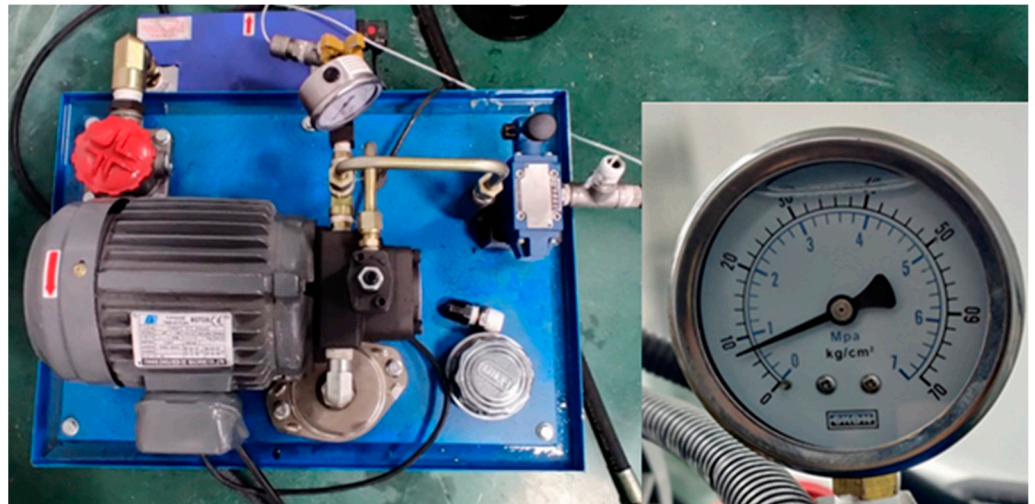


Figure 5. Oil tank and oil pressure gauge.

3. Experimental Analysis at Different Oil Pressure Levels

During the high-speed operation of a rotor-sliding bearing, the oil film pressure inside the bearing not only supports the rotation of the rotor shaft but also dissipates heat and prevents direct contact between the journal and the shaft tile, so the oil film pressure plays an important role in the stable operation of the sliding bearing, and the influence of the oil pressure of the sliding bearing inlet pipe on the internal oil pressure distribution cannot be ignored. Most of the studies only focus on the oil film pressure distribution between the journal and the shaft tile. There is less research on the operating characteristics of the rotor system, so it is also necessary to analyze the influence of this important parameter on the operational stability.

The sliding bearing of the rotor test bench is connected to the oil inlet pipe and the oil outlet pipe to form a self-circulating oil system. In the oil pressure circulation, it is necessary to make a good seal at the bearing support to avoid overflow under excessive oil pressure and high speed. During the experiment, the ideal oil pressure value is selected by mediating the throttle valve and observing the change of the hydraulic gauge size to achieve low pressure and low flow rate oil circulation lubrication.

The main objective of this paper is to study the dynamic response of the sliding bearing system at different oil pressure levels. Therefore, several experimental tests are carried out under the oil pressure of 0.2~1.2 MPa with different rotational speeds. The analyses are presented according to the experimental results extracted by the acceleration sensor and eddy current sensor. In addition, the acceleration and deceleration processes of the test system are conducted at a lower oil pressure level.

3.1. Single Rotor Experimental Analysis

Figure 6a,b show the vertical amplitude variation of the amplitude at the turntable with the speed change under the inlet oil supply pressure of 0.2 MPa and 1.0 MPa, respectively. The system vibration response at 1.0 MPa oil supply pressure reflects that: the amplitude value fluctuates more at medium and high speeds, the overall amplitude value changes increase with the increase in speed, and the amplitude value fluctuates significantly at high speeds. Compared with the system response at different oil pressures, the minimum difference in amplitude does not exceed 6 mm, and the maximum difference in amplitude is about 28 mm, which shows that the difference in amplitude of the system amplitude at different oil pressures is small.

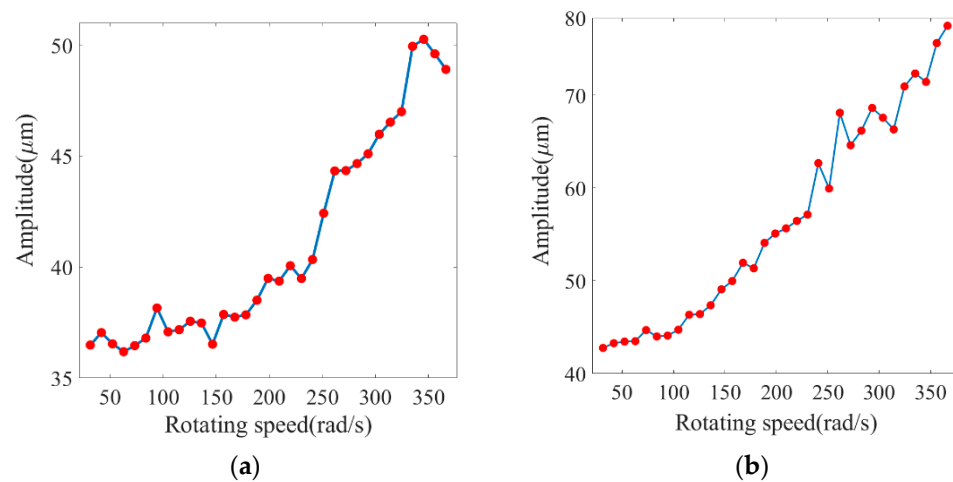


Figure 6. Variation diagram of system amplitude under different oil pressure. (a) Oil pressure level of 0.2 MPa. (b) Oil pressure level of 1.0 MPa.

3.1.1. Oil Pressure Level of 0.2 MPa

To get a clearer picture of the form of the motion, Jules Henri Poincaré intercepts the trajectory of a continuous motion with a cross-section called the Poincaré section. The shape of the motion can be succinctly determined by the trajectory passing through the section, and the resulting image is called the Poincaré map.

Figure 7 shows the Poincaré mapping and spectrum at the supply pressure of 0.2 MPa, and the rotational speeds are 100 rad/s , 210 rad/s , and 335 rad/s . The Poincaré cross-sectional maps at different rotational speeds are almost closed and nearly circular, indicating that the system has no periodic solution and is basically in the proposed periodic operation. The main frequency in the spectrum rises with the rotational speed. There is no obvious change in the spectrum with the increase of rotational speed. A small 2-fold frequency appears due to the mass eccentricity and self-excited vibration of the test bench itself at a high rotational speed.

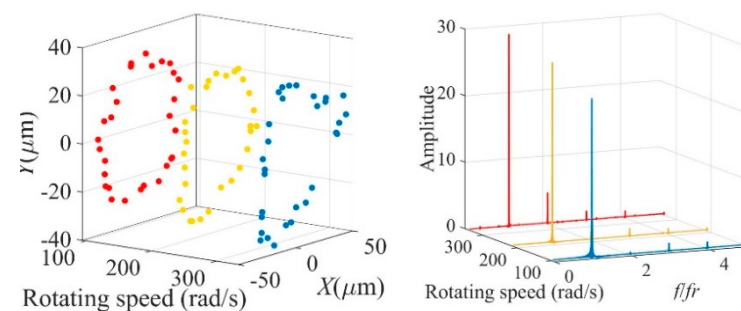


Figure 7. System response at different speeds when the oil pressure is 0.2 MPa.

3.1.2. Oil Pressure Level of 1.0 MPa

Figure 8 shows the Poincaré mapping and spectrum at the oil supply pressure of 1.0 MPa, and the speeds are 100 rad/s , 210 rad/s , and 335 rad/s . When the oil supply pressure becomes larger, the Poincaré mapping shows multiple scattered concentrated curve segments, and the cycle state increases as the speed rises, but the multi-cycle operation is shown throughout the speed state. The main frequency component of the system increases, and the remaining multiplicative frequency component does not appear. In summary, the system response at the two oil pressures shows that the vibration amplitude and main frequency of the rotor system at higher oil pressure increase, but the periodic response is simple, and the system as a whole is in a more stable periodic state.

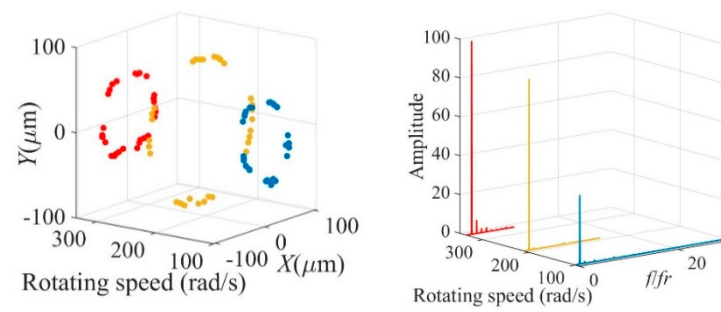


Figure 8. System response at different speeds when the oil pressure is 1.0 MPa.

3.2. Dual-Rotor Experimental Analysis

In order to elucidate the effect of different oil pressure levels on the dynamic response of the plain bearing system under a dual rotor system, a rotor test stand with dual-rotor sliding bearings was developed independently. Three oil pressure levels of 0.2 MPa, 0.75 MPa, and 1.2 MPa were tested, respectively. The specific operating conditions and operational conditions of the double rotor test stand were similar to those of the single rotor test stand. The critical speed of the dual-rotor test bench is about 480 rad/s by simulating the operating mode of the rotor test bench. Figure 9 shows the vertical three-dimensional spectral waterfall of the dual-rotor test bench under normal operating conditions. The vibration amplitude gradually increases with the increase of the speed, and a certain speed amplitude suddenly decreases. Continue to increase the speed can see the obvious oil whirl phenomenon.

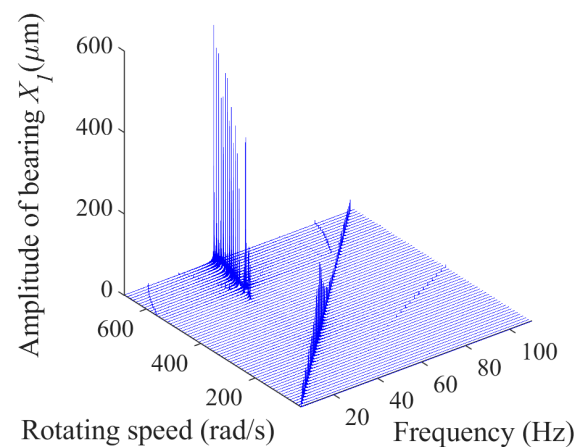


Figure 9. Three-dimensional spectrum waterfall diagram of a dual-rotor system.

3.2.1. Oil Pressure Level of 0.2 MPa

Figure 10 shows the frequency waterfall chart extracted by the rotating disk along the vertical direction with a higher oil pressure level of about 0.2 MPa. Figure 11 shows the rotating shaft along the same direction with a higher oil pressure level of about 0.2 MPa. In terms of the results presented in Figures 10 and 11, the vibration amplitude gradually increases with the increment of the rotating speed in the range of 0 to 283 rad/s. The amplitude is abruptly dropped when the rotating speed exceeds 283 rad/s. Accelerating the speed up to 480 rad/s, the amplitude is significantly characterized by a half doubling frequency, which means the rotor has converted to the status of oil whip, and the component of the amplitude corresponding to the half doubling frequency is gradually elevated.

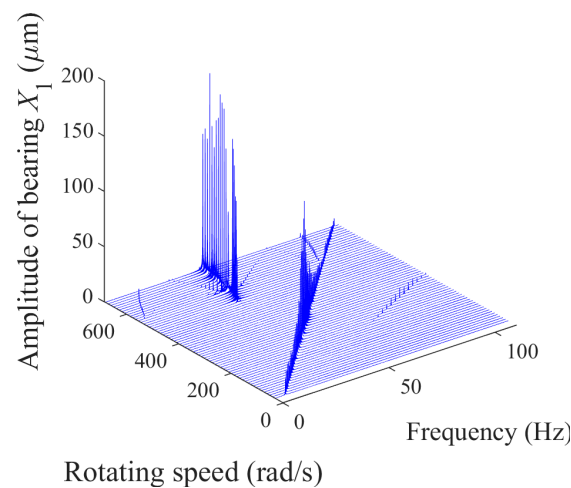


Figure 10. Frequency waterfall chart of the rotating disk along a vertical direction at oil pressure of 0.2 MPa.

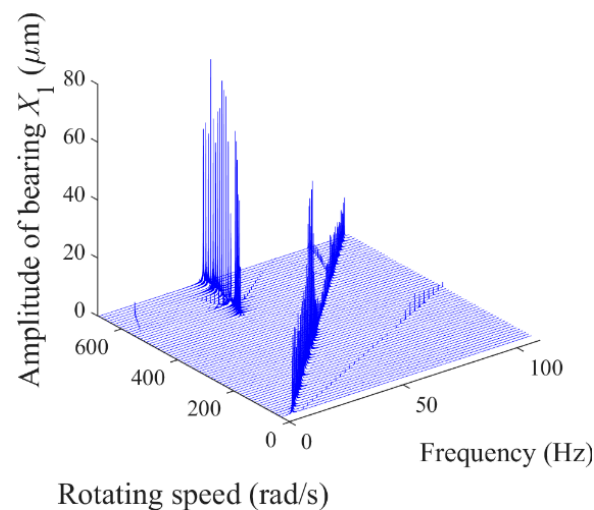


Figure 11. Frequency waterfall chart of the rotating shaft along a vertical direction at oil pressure of 0.2 MPa.

Figures 12 and 13 show that with a higher oil pressure level of about 1.2 MPa, the trajectory of the shaft center with the Poincaré map and the power spectrum for the rotating disk and the shaft at different rotating speeds. At lower rotating speeds, the trajectory of the disk is visualized in oval, while the track of the shaft displays a quasi-circle. The distribution of the Poincaré map indicates that the rotor system features a multicycle under operation, which is also confirmed by the figure of the power spectrum where the amplitude reaches the maximum only at the frequency equaling to the rotating frequency (1.0 fr).

Accelerating the speed to the status of the oil whip, the whirl orbits of the disk and the shaft are both disorderly, and the scattered points are distributed discretely and irregularly in the Poincaré map. The rotor motion cycle changes under different oil pressures, as shown in Table 1. Except for the domain frequency equaling to the rotating frequency, the amplitude at the frequency of double rotating frequency is also remarkable, and the amplitude for the disk is higher than that of the shaft. From what has been discussed above, the rotor system is in a chaotic state at this time.

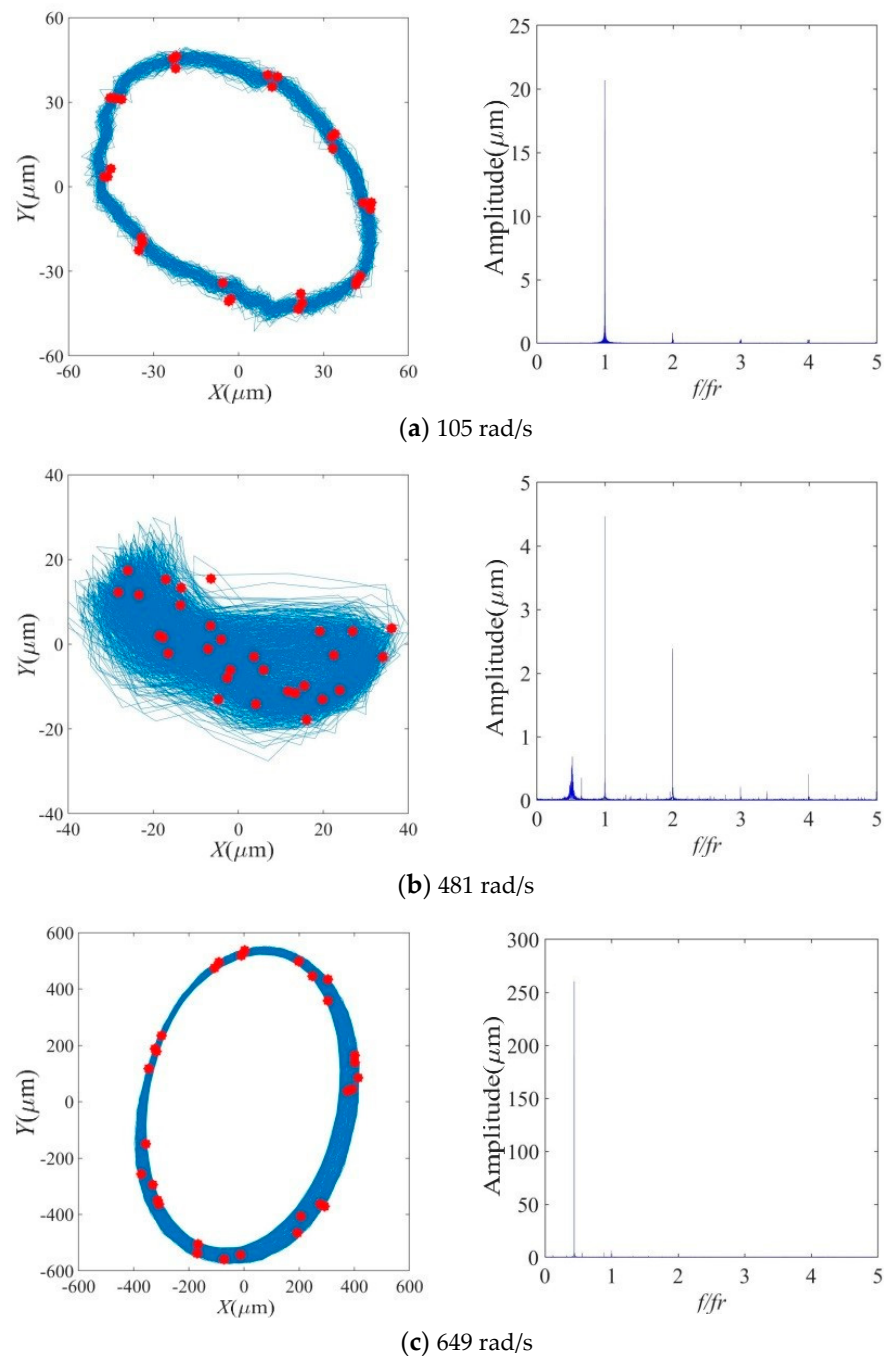


Figure 12. Trajectory of shaft center with the Poincaré map (left side) and the power spectrum (right side) for the rotating disk at different rotating speeds.

At the test condition in the vicinity of the maximum rotating speed, the whirl orbits of the disk and the shaft feature oval in shape. In addition, the radius of the trajectory is the maximum among the three speeds in Figures 12 and 13. Compared with the frequency characteristic at lower speeds, the domain frequency at 649 rad/s is calculated as half of the rotating frequency. At the same time, all amplitudes at the three test conditions are comparable. The analysis results can give some insight into that the system of the rotor test operates in quasi-periodic mode.

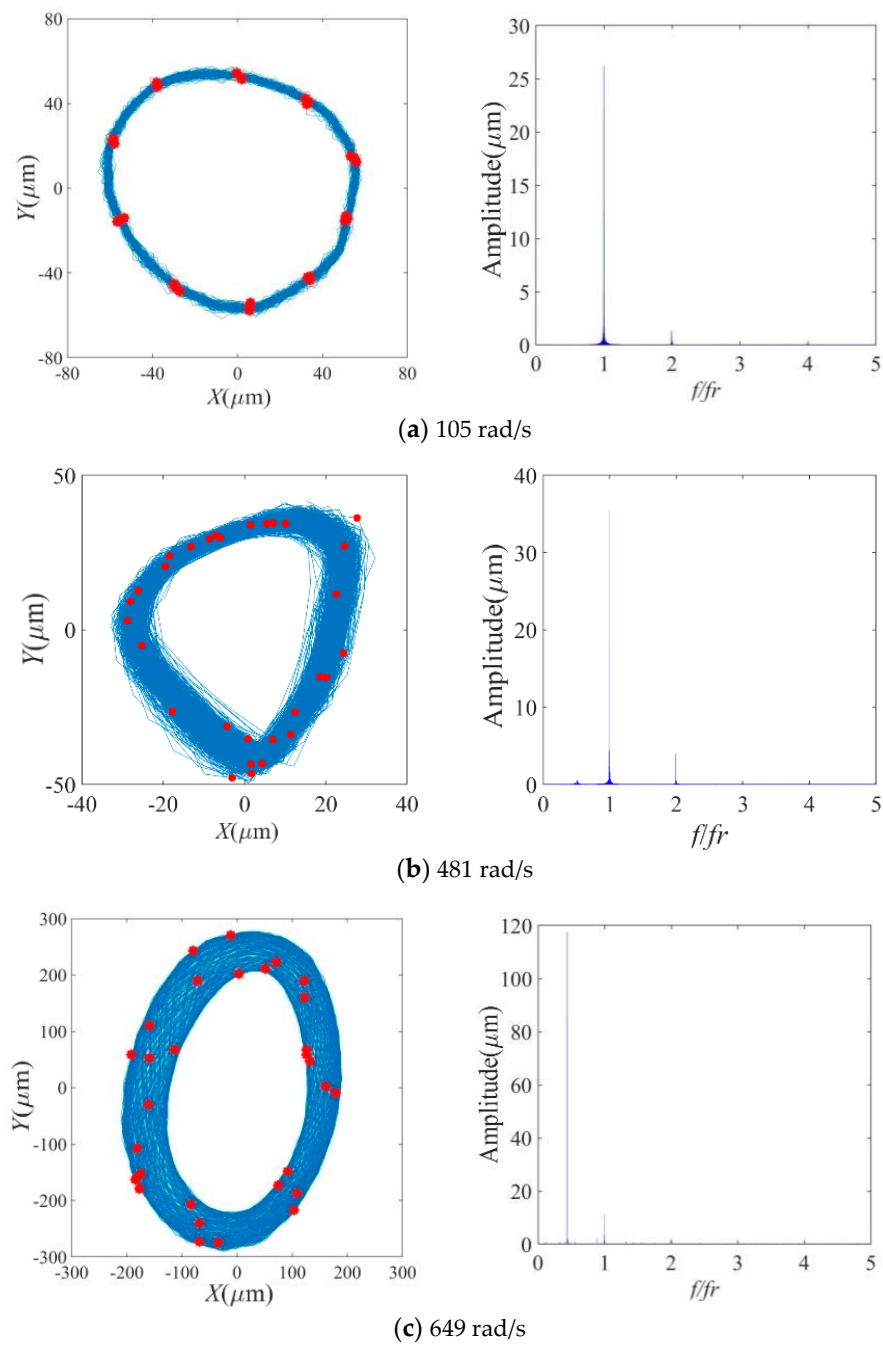


Figure 13. Trajectory of shaft center with the Poincaré map (left side) and the power spectrum (right side) for the rotating shaft at different rotating speeds.

Table 1. Rotor periodic motion as the speed rises under different oil pressures.

Rad/s	178	481	649
Oil Pressure			
0.2 MPa	Period-10	Chaos	Period-7
0.75 MPa	Quasi-periodic	Chaos	Chaos
1.2 MPa	Period-4	Quasi-periodic	Quasi-periodic

3.2.2. Oil Pressure Level of 0.75 MPa

The frequency waterfall chart for the disk and shaft at the oil pressure level of 0.75 MPa are described in Figures 14 and 15 which show the trend and relative higher variation of

the amplitude with the rotating speed and frequency is similar to the oil pressure level of 0.2 MPa. However, the amplitudes in Figures 14 and 15 are more powerful, and the starting frequencies entering the status of oil whip are both 481 rad/s.

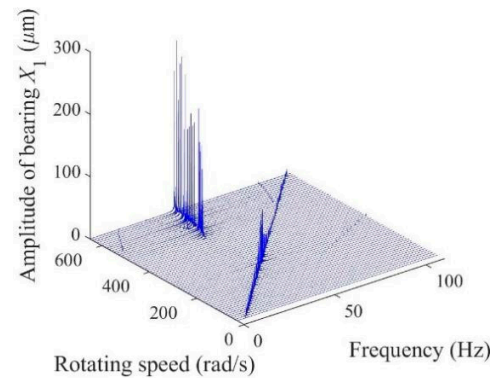


Figure 14. Frequency waterfall chart of the rotating disk along a vertical direction at oil pressure of 0.75 MPa.

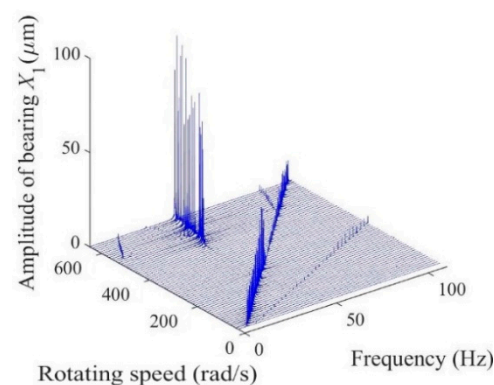


Figure 15. Frequency waterfall chart of the rotating shaft along a vertical direction at oil pressure of 0.75 MPa.

The whirl orbit, together with the Poincaré map and the results of the power spectrum for the disk and the shaft at the oil pressure level of 0.75 MPa, are shown in Figures 16 and 17. At the condition of lower rotating speed, the vibration of the whirl orbit is increased with the lift of the oil pressure. The point regularly placed on the Poincaré map, and the trajectory coincide generally. The whirl orbit for the disk and the shaft show crescent in shape, respectively, at 481 rad/s and 377 rad/s, which means that the degree of misalignment of the rotor system increases. However, the minimum amplitudes are captured at this condition, and the amplitude at the double frequency rotating frequency is remarkable. The most drastic amplitudes are predicted at the rotating speed of 670 rad/s, the domain frequency of the trajectory vibration is determined as 0.5 times the rotating frequency, and the amplitude for the disk is almost three times that at the shaft. The whirl orbit is more rounded and shown as a standard ellipse, the points in the Poincaré map are clearly concentrated on the fourth quadrant of the whirl orbit. Therefore, the increment of the oil from 0.2 MPa to 0.75 MPa is inclined to improve the stability of the rotor system.

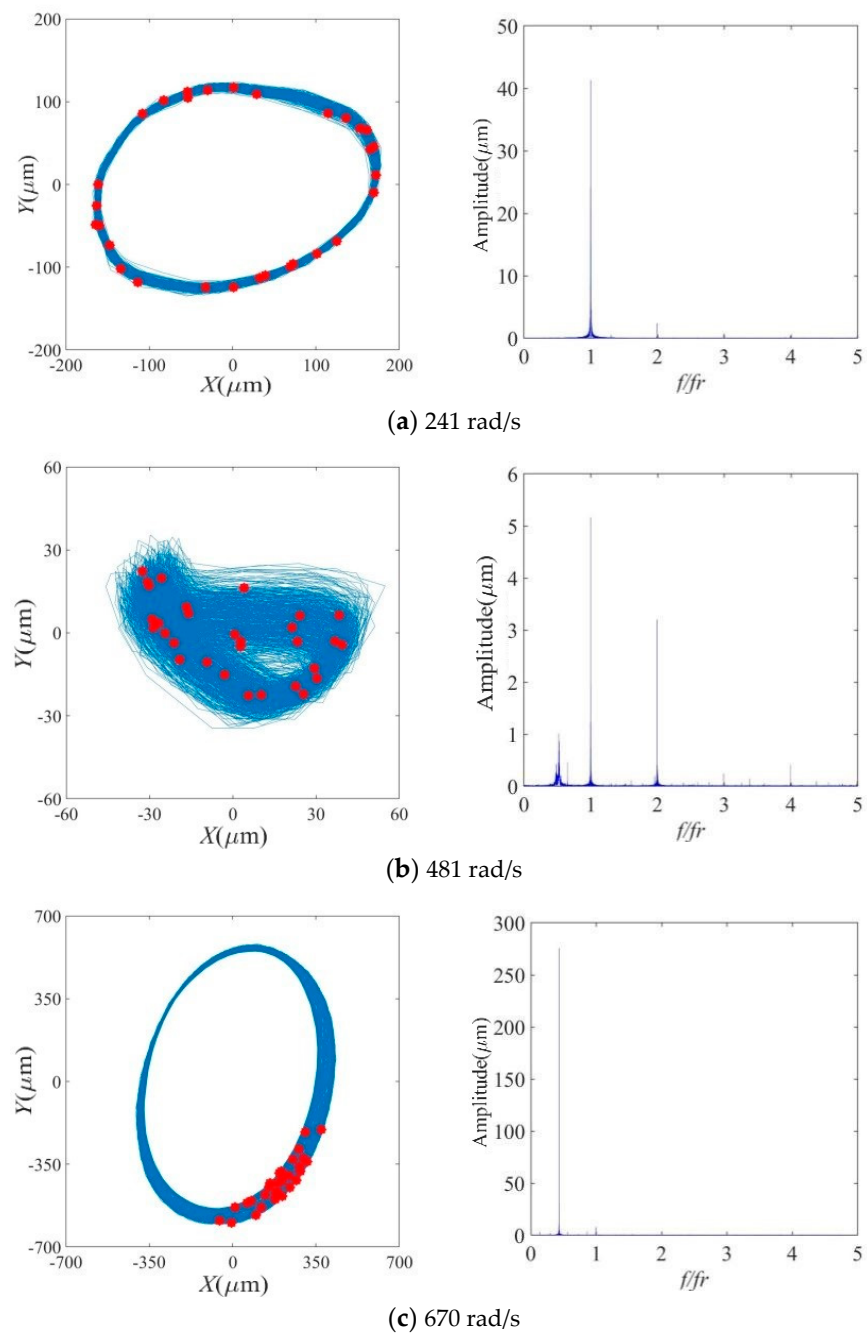


Figure 16. Trajectory of shaft center with the Poincaré map (left side) and the power spectrum (right side) for the rotating disk at different rotating speeds and oil pressure of 0.75 MPa.

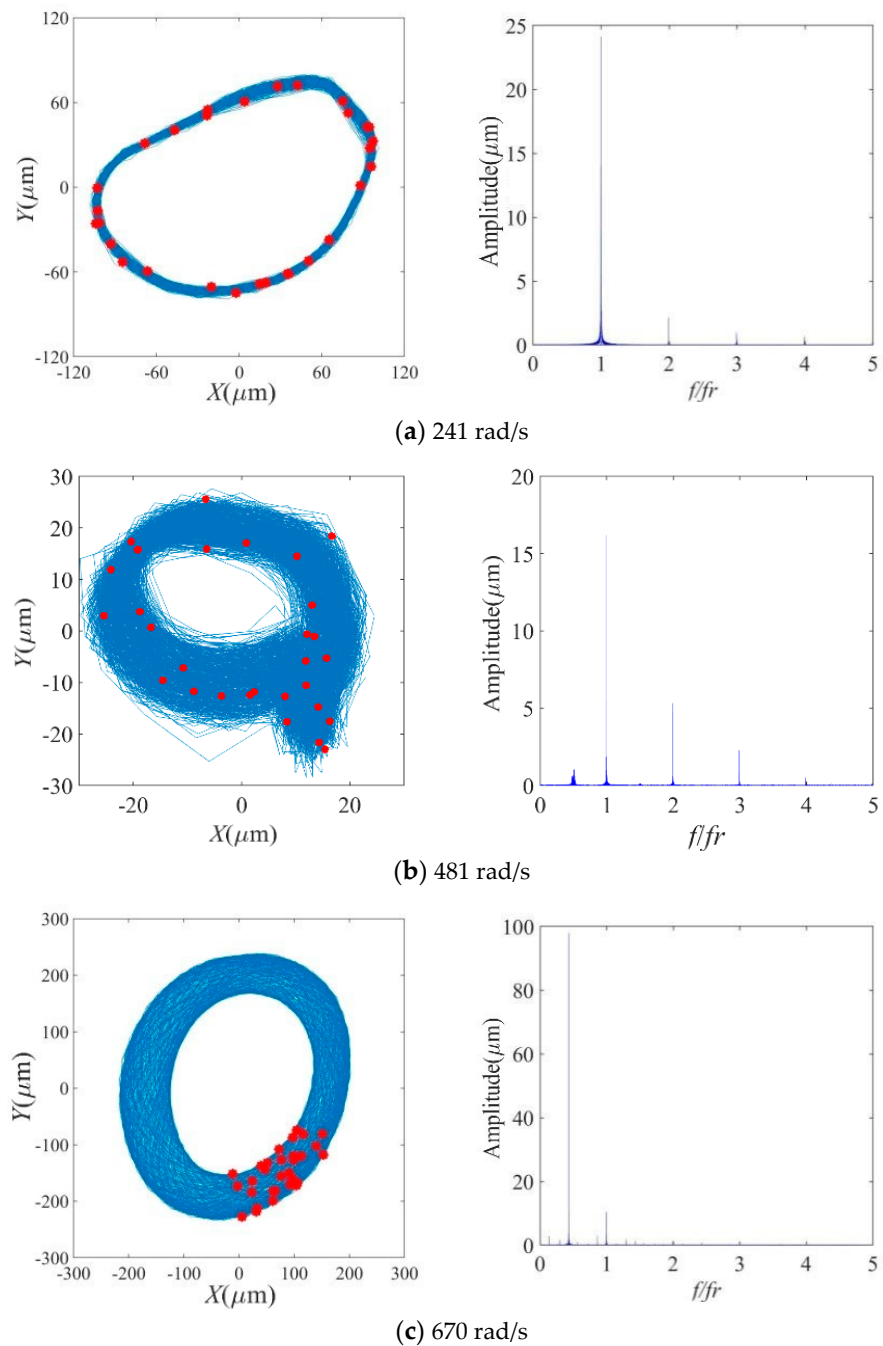


Figure 17. Trajectory of shaft center with the Poincaré map (**left side**) and the power spectrum (**right side**) for the rotating shaft at different rotating speeds and oil pressure of 0.75 MPa.

3.2.3. Oil Pressure Level of 1.2 MPa

To show the frequency and amplitude characteristics of the condition with a higher oil pressure level of about 1.2 MPa, the frequency waterfall chart of the disk and the shaft are visualized in Figures 18 and 19. The results highlight that the frequencies featuring the oil whip are determined as 471 rad/s, where a sharp rise of amplitude is captured both for the rotating disk and shaft.

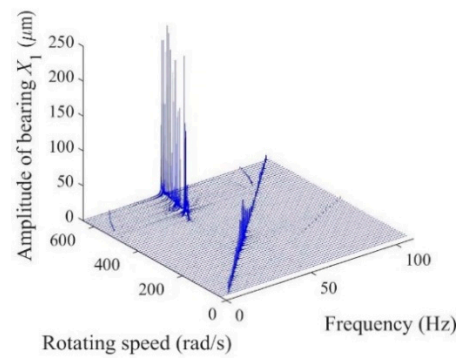


Figure 18. Frequency waterfall chart of the rotating disk along a vertical direction at oil pressure of 1.2 MPa.

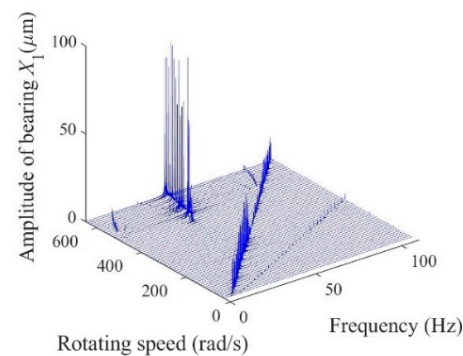


Figure 19. Frequency waterfall chart of the rotating shaft along a vertical direction at oil pressure of 1.2 MPa.

Figures 20 and 21 depict the higher oil pressure level of about 1.2 MPa, the whirl orbit overlay blending with the Poincaré map, as well as the information on the power spectrum for the disk and the shaft. At the minimum rotating speed of 178 rad/s, the whirl orbit shows as a shape with a standard circle, and the points representing the Poincaré map regularly spaced by 90° are placed and projected on the whirl orbit. At the rotating speed of 481 rad/s where the oil whip is first induced, the whirl orbit is more inconsistent and shows an irregular shape. However, the vibration amplitude at the rotation frequency decreases sharply. At the condition where the oil whip is fully developed, the vibration amplitude is abnormally high. The whirl orbit is a regular elliptic ring, and the Poincaré points are also projected on the range of the whirl orbit.

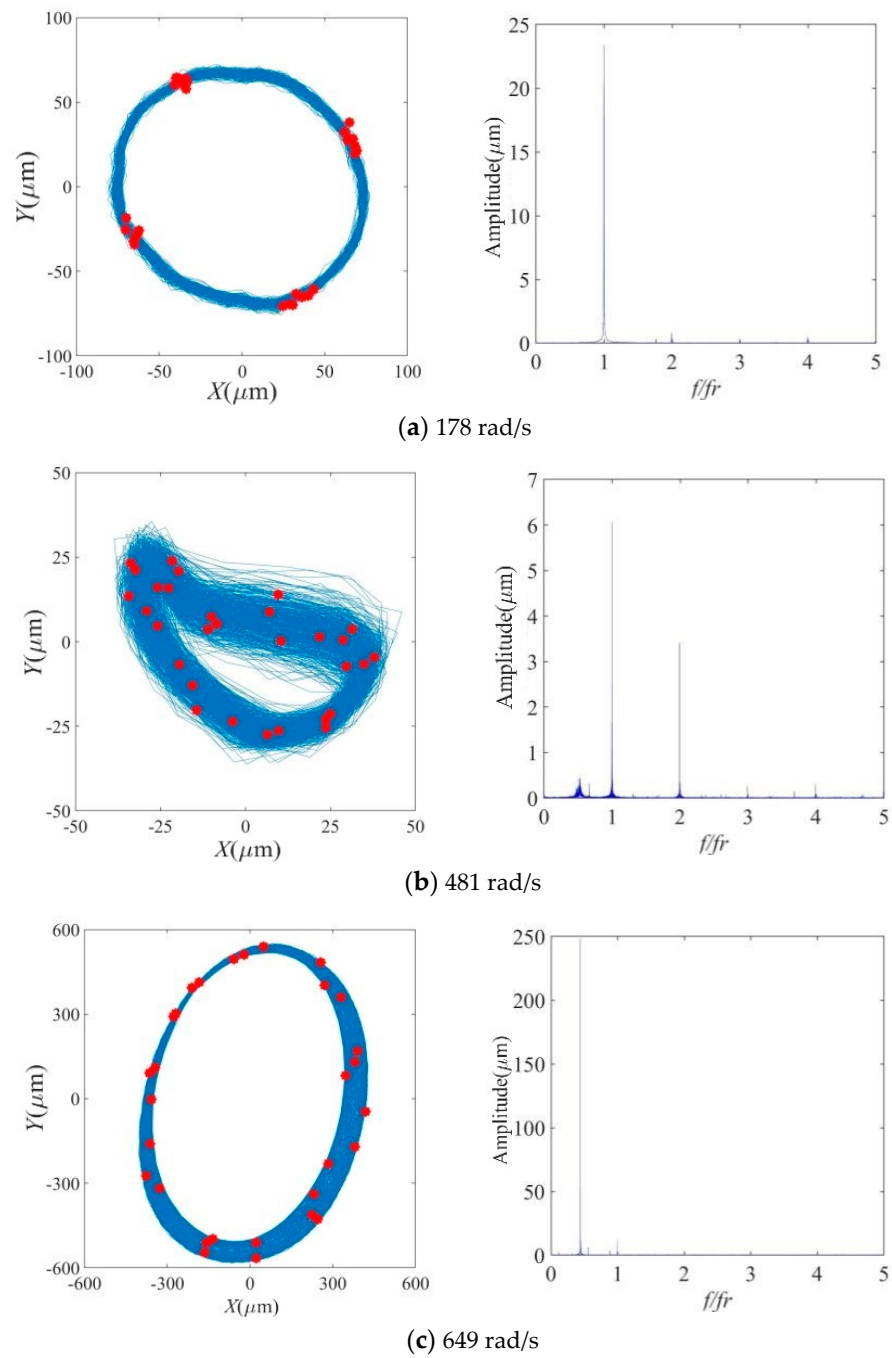


Figure 20. Trajectory of shaft center with the Poincaré map (left side) and the power spectrum (right side) for the rotating disk at different rotating speeds and oil pressure of 1.2 MPa.

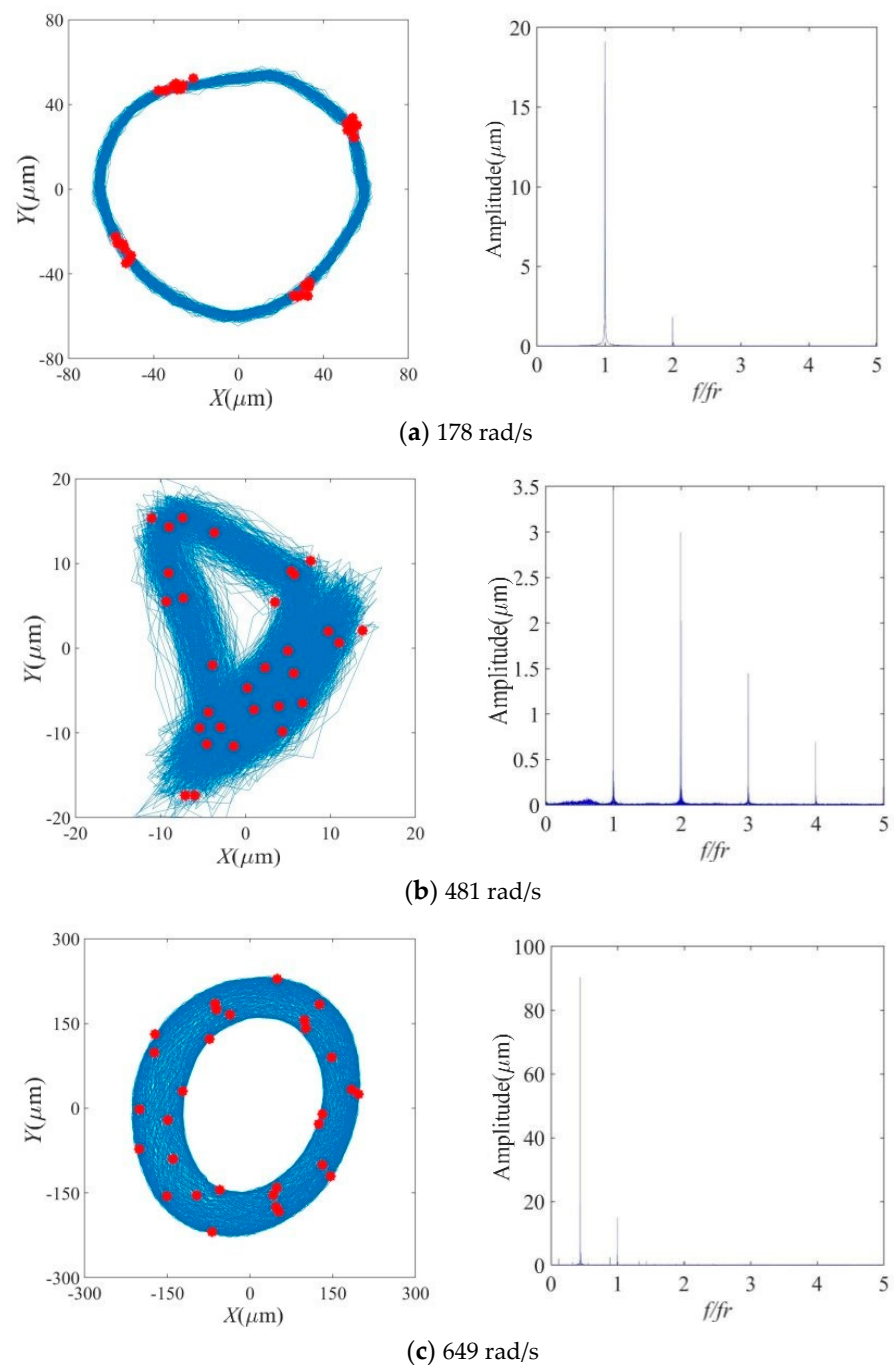


Figure 21. Trajectory of shaft center with the Poincaré map (left side) and the power spectrum (right side) for the rotating shaft at different rotating speeds and oil pressure of 1.2 MPa.

3.2.4. Time Domain Information of Speed Variation Processes

Figure 22 indicates the time-resolved vibration amplitude in the rotating disk during the processes of variable speed at the oil pressure level 0.2 MPa. The designed ratio of speed variation is, respectively, 200 r/s and 300 r/s for the test rig. As depicted in Figure 22, one can observe an abrupt rise and fall for the vibration amplitude, which means some faults for the test rig. The time instant corresponding to the sudden rising amplitude during the acceleration process is 26.79 s, while it is 10.17 s for the deceleration process. Therefore, the rotating speeds at the time instant where amplitudes change abruptly are 519 rad/s and 366 rad/s, respectively, for the acceleration process and deceleration process. As a consequence, the oil whip is suddenly stimulated and damped, as well as influenced by the

inertia effect. Namely, the rotating speed corresponding to oscillation induction during the process of speed rising is larger than that of the oscillation disappears when the speed is decreased. However, it is not the oil whip at the speed of 366 rad/s during the deceleration process. While it is actually the phenomenon of the oil whip. In addition, the deceleration process is conducted by turning off the motor of the rotor test rig, which may lead to a slight offset. On all accounts, the inertia effect is prevalent for the deceleration process, and the rotating speed exciting oil whip for the acceleration process is larger than that of the deceleration process.

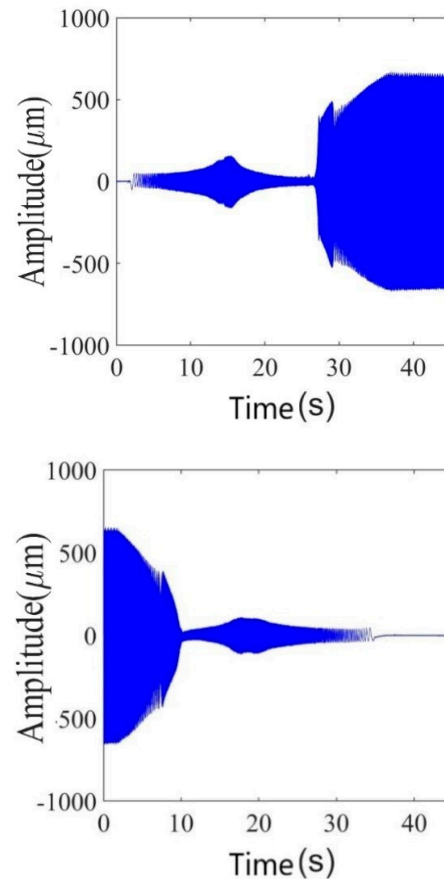


Figure 22. Time-resolved vibration amplitude in the rotating disk during the processes of acceleration and deceleration at the oil pressure level 0.2 MPa.

3.2.5. Discussion and Further Analyses

From the analysis of the results of the dual-rotor test stand, it is clear that: the maximum speed of the rotor system in the dual-rotor test stand is 680 rad/s, and the sampling frequency of the acquisition system is 1024 Hz. a significant vibration amplitude is generated around 481 rad/s, and the frequency increases by half, which is consistent with the critical speed of the test stand under test, and the rotor system starts to change to oil whirl motion.

At lower speeds, the whirl orbit is relatively regular and quasi-circular in shape, while the Poincaré points are regularly placed on the whirl orbit. When the rotational speed is increased to the critical speed for generating oil whirl motion, irregular axial trajectories are observed. Although Poincaré points are also projected on the whirl orbit, they are disordered. Near the maximum rotational speed, the whirl orbit shows an elliptical shape, and the Poincaré points tend to be regularly distributed. When the oil whirl motion is fully developed, the amplitude of the rotor system increases abnormally and accordingly, the radius of the whirl orbit increases. In addition, the results of the velocity variation process indicate that the oil whip is suddenly stimulated and damped and subject to inertial effects.

4. Concluding Remarks

In this paper, the vibration response of single-rotor and dual-rotor systems is analyzed by varying different oil feed pressures. On the single-rotor test bench: Two oil pressure levels of 0.2 MPa and 1.0 MPa were tested, respectively. The single-rotor system is operated at a stable speed range below the speed of 31~366 rad/s. The increase of oil pressure induces the rotor system amplitude to become larger, the radius of the whirl orbit at the monitoring point becomes larger, the octave amplitude in the spectrum also grows, and the system operates under the larger oil pressure of about 1.0 MPa is mostly periodic and more stable. Dual-rotor test bench: Three oil pressure levels of 0.2 MPa, 0.75 MPa, and 1.2 MPa were tested, respectively. Low oil pressure is about 0.2 MPa on the system operating state of more than the vortex speed, with the increase in oil pressure of about 1.2 MPa, the rotor operating speed is less than the critical speed, the system motion cycle simple, and no excess frequency components. The rotor test bench is a comprehensive test bench for multi-fault simulation and analysis. There are many effects of filtering and self-excited vibration in the rotor system during normal operating conditions without faults. The single-rotor test bench is operated at a stable speed range below the critical speed, and the system amplitude is selected to increase slightly by 1.0 MPa compared with the low inlet pressure, which is beneficial to the stability of the subsequent experiments. The influence of the oil feed pressure on the stability of the rotating system studied in this paper provides some reference for the researchers to study the rotating component support system of the rotating machinery later.

Author Contributions: Conceptualization, Z.F. and W.S.; methodology, Q.D. and Y.C.; software, Z.F.; validation, Z.F. and W.S.; investigation, Q.D. and Y.C.; writing—original draft preparation, Z.F. and Q.D.; writing—review and editing, W.S.; supervision, W.S. All authors have read and agreed to the published version of the manuscript.

Funding: This research was funded by the National Natural Science Foundation, grant number 52179089.

Institutional Review Board Statement: Not applicable.

Informed Consent Statement: Not applicable.

Data Availability Statement: Not applicable.

Conflicts of Interest: The authors declare no conflict of interest.

References

1. Holmes, J.D. Mean and fluctuating internal pressures induced by wind. *Wind. Eng.* **1980**, *1*, 435–450.
2. Sharma, R.N. Internal Pressure Dynamics with Internal Partitioning. In *Proceedings of the Eleventh International Conference on Wind Engineering*; International Association for Wind Engineering (IAWE): Lubbock, TX, USA, 2003; pp. 112–116.
3. Stathopoulos, T.; Luchian, H.D. Transient Wind-Induced Internal Pressures. *J. Eng. Mech.* **1989**, *115*, 1501–1514. [[CrossRef](#)]
4. Vickery, B.J.; Bloxham, C. Internal pressure dynamics with a dominant opening. *J. Wind Eng. Ind. Aerod.* **1992**, *41*, 193–204. [[CrossRef](#)]
5. Chen, Z.; Jiao, Y.; Xia, S.; Huang, W.; Zhang, Z. An Efficient Calculation Method of Nonlinear Fluid Film Forces in Journal Bearing. *Tribol. Trans.* **2002**, *45*, 324–329. [[CrossRef](#)]
6. Qin, P.; Meng, Z.Q.; Zhu, J. BP Network Model for Nonlinear Oil-film Force on Hydrodynamic Bearing. *Mocaxue Xuebao/Tribol.* **2002**, *22*, 226–231. (In Chinese)
7. Wang, W.; Zhang, Z. Calculation of journal dynamic locus aided by database of non-stationary oil film force of single bush segment. *Asia-Pac. Vib. Conf.* **1993**, *93*, 365–369.
8. Meng, Z.Q.; Hua, X.U.; Zhu, J. A Database Method of Nonlinear Oil Film Force Based on Poincare Transformation. *Tribology* **2001**, *21*, 223–227. (In Chinese)
9. Hei, D.; Zheng, M.R. Approximate solution of nonlinear oil film forces of finite length slide journal bearing by considering oil inlet hole. *J. Mech. Electr. Eng.* **2016**, *33*, 1315–1321. (In Chinese)
10. Kang, N.; Chi, Q.M. Calculation of oil film bearing capacity of Journal Bearing Based on N-S equation. *Lubr. Eng.* **2010**, *35*, 9–12. (In Chinese)
11. Qin, P.; Shen, Y.; Xu, H.; Zhu, J. Nonlinear oil-film force database of journal bearing including inlet pressure. *Mocaxue Xuebao/Tribol.* **2004**, *24*, 258–262. (In Chinese)

12. Yu, G.C.; Liu, S.L.; Zheng, S.Y. Performance analysis of double oil groove circular Bush sliding bearing under disturbance. *J. Vib. Shock*. **2012**, *31*, 46–49. (In Chinese)
13. Gao, Q.S.; Yang, J.G. Study on dynamic characteristics of hydrodynamic sliding bearing based on CFD method. *Lubr. Eng.* **2008**, *33*, 65–67. (In Chinese)
14. Yang, J.; Yang, K.; Yu, D.; Fu, Z.; Liu, Z. Study on nonlinear oil film force of sliding bearing. *J. Vib. Eng.* **2005**, *18*, 123–128. (In Chinese)
15. Shi, Y.; Zhang, C.; Ren, L.; Zhang, L.; Peng, L. Pressure distribution and dynamic characteristic coefficient of sliding bearing. *J. Harbin Eng. Univ.* **2011**, *32*, 1134–1139. (In Chinese)
16. Li, N.E.; Wang, L. Effect of oil inlet hole scheme on lubrication characteristics of sliding bearing of gear driven turbofan engine. *Lubr. Eng.* **2018**, *43*, 63–68. (In Chinese)
17. Wang, J.K.; Khonsari, M.M. Effects of Oil Inlet Pressure and Inlet Position of Axially Grooved Infinitely Long Journal Bearings, Part II: Nonlinear Instability Analysis. *Tribol. Int.* **2008**, *41*, 132–140. [[CrossRef](#)]
18. Liu, Z.M.; Yue, G.J.; Shen, F. Numerical simulation of carrying capacity in hydrostatic oil cavity under different inlet Reynolds numbers. *Beijing Gongye Daxue Xuebao/J. Beijing Univ. Technol.* **2013**, *39*, 965–970. (In Chinese)
19. Goryunov, L.V.; Takmovtsev, V.V.; Ignat'ev, D.V.; Erzikov, A.M. Influence of an oil supply process on the characteristics of plain journal bearings. *Russ. Aeronaut.* **2012**, *55*, 39–41. [[CrossRef](#)]